We are IntechOpen, the world's leading publisher of Open Access books Built by scientists, for scientists

4,800
Open access books available

122,000
International authors and editors

135M
Downloads

Our authors are among the

154
Countries delivered to

TOP 1%
most cited scientists

12.2%
Contributors from top 500 universities

WEB OF SCIENCE™

Selection of our books indexed in the Book Citation Index in Web of Science™ Core Collection (BKCI)

Interested in publishing with us?
Contact book.department@intechopen.com

Numbers displayed above are based on latest data collected.
For more information visit www.intechopen.com

12

Hyperspectral Remote Sensing – Using Low Flying Aircraft and Small Vessels in Coastal Littoral Areas

Charles R. Bostater, Jr., Gaelle Coppin and Florian Levaux
Marine Environmental Optics Laboratory and Remote Sensing Center, College of Engineering, Florida Institute of Technology, Melbourne, Florida USA

1. Introduction

Large field of view sensors as well as flight line tracks of hyperspectral reflectance signatures are useful for helping to help solve many land and water environmental management problems and issues. High spectral and spatial resolution sensing systems are useful for environmental monitoring and surveillance applications of land and water features, such as species discrimination, bottom top identification, and vegetative stress or vegetation dysfunction assessments[1]. In order to help provide information for environmental quality or environmental security issues, it is safe to say that there will never be one set of sensing systems to address all problems. Thus an optimal set of sensors and platforms need to be considered and then selected. The purpose of this paper is to describe a set of sensing systems that have been integrated and can be useful for land and water related assessments related to monitoring after an oil spill (specifically for weathered oil) and related recovery efforts. Recently collected selected imagery and data are presented from flights that utilize an aircraft with a suite of sensors and cameras. Platform integration, modifications and sensor mounting was achieved using designated engineering representatives (DER) analyses, and related FAA field approvals in order to satisfy safety needs and requirements.

2. Techniques

2.1 Imaging systems, sensor systems and calibration

Sensors utilized have been: (1) a photogrammetric 9 inch mapping camera utilizing a 12 inch focal length cone, and using AGFA X400PE1 color negative film that has been optimized for high resolution scanning (2400 dpi) in order to reduce the effects of newton rings and an associated special glass plate from Scanatronics in the Netherlands; (2) forward and aft full high definition (HD) video cameras recording to solid state memory with GPS encoding; (3) a forward mounted Nikon SLR 12.3 megapixel digital camera with a vibration reduction zoom lens and GPS encoding; (4) a high hyperspectral imaging system with 1376 spatial pixels and 64 to 1040 spectral bands.

The HSI imaging system utilizes a pen tablet computer with custom software. The HSI pushbroom system is integrated into the computer with an external PCMCIA controller card for operating the temperature stabilized monochrome camera which is bore sighted with a transmission spectrograph and ~39 degree field of view lens. The HSI imaging system is gimbal mounted and co-located with one of the HD 30 HZ cameras. The HSI system runs between ~20 to 90 HZ and is also co-located with a ~100 HZ inertial measurement unit (IMU). The IMU is strap down mounted to the HSI along the axis of view of the hyperspectral imager.

An additional 5HZ WAAS GPS output is recorded as another data stream into the custom software that allows on the fly changes to the integration time and spectral binning capability of the system. The HSI system is calibrated for radiance using calibration spheres and with spectral line sources for wavelength calibration. Flights are conducted with the 5 cameras in a fashion to allow simultaneous and or continuous operation with additional use of camera intervalometers that trigger the Nikon and photogrammetric camera. Examples of imagery taken on March 21, 2011 are shown below as well as spectral signatures and in-situ field targets that are typically utilized for processing imagery for subsurface or submerged water feature detection and enhancements.

Airborne imagery shown in this paper was collected at 1,225 m between 10 AM local time or 4 PM local, with a 1/225 second shutter speed and aperture adjusted for optimal contrast and exposure. The large format (9 in^2) negatives scanned at 2400 dpi using a scanner and a special glass plate obtained from Scanatron, Netherlands allows for minimization of "newton rings" in the resulting ~255 megapixel multispectral imagery shown below (left image). Experience has shown that this method works well with AGFA X400PE1 film. The aerial negative scanning process is calibrated using a scanned target with known sub-millimeter scales 0.005 mm to 5 um resolution using a 2400 dpi scanner. The film scanning process results in three band multispectral images with spectral response curves published by the film manufacturer (Agfa or Kodak).

*In-sit*u targets as shown in Figure 1 are used for calibration of the imagery using a combination of white, black or gray scale targets as shown below in an airborne digital image (right). Airborne targets are used for calibrating traditional film and digital sensor data for spatial and spectral characteristics using *in-situ* floating targets in the water as shown below.

Targets (figure 2) are placed along flight lines. These types of land and water targets are used for image enhancement techniques, for use as GPS georeferencing ground control points, and georeferencing accuracy assessments. They are necessary in order to assess shoreline erosion estimation resulting from oil spill impacts along littoral zones.

Figure 2 below shows images of weather oil taken in the Jimmy Bay area in January, 2011, eight months after the major spill was contained in the deep waters of the northern Gulf of Mexico.

2.2 Pushbroom imagery corrections for aerial platform motions

Airborne pushbroom imagery collected aboard moving platforms (ground, air, sea, space) requires geometric corrections due to platform motions. These motions are due to changes in the linear direction of the platform (flight direction changes), as well as sensor and platform motion due to yaw, pitch and roll motions. Unlike frame cameras that acquire a 2 dimensional image, pushbroom cameras acquire one scan line at a time. A sequence of

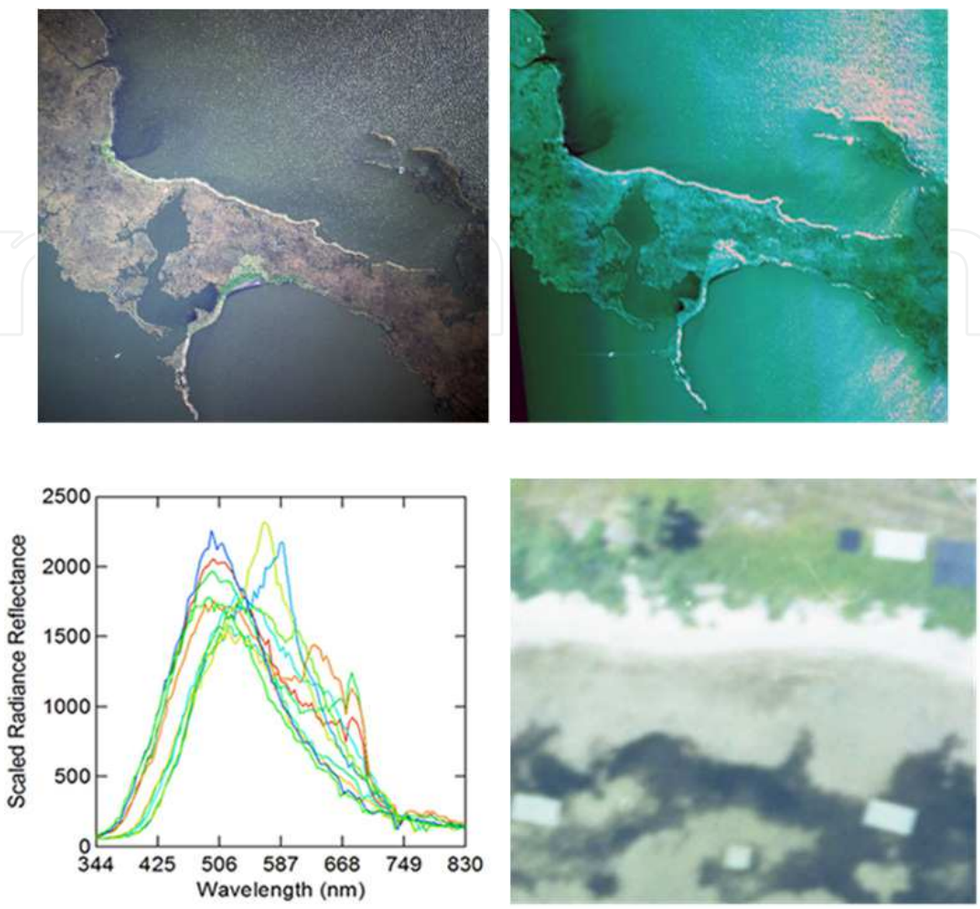

Fig. 1. Image (upper left) of a scanned AGFA color negative film (X400PE1) from an airborne flight March 21, 2011 over Barataria Bay, LA. The upper right image is a simultaneously collected hyperspectral RGB image (540, 532, 524 nm). Imagery indicates the ability to detect weathered oil in the area from oil spill remediation activities. The graph shows selected spectra in weathered oil impact areas. The lower right shows in-situ targets.

Fig. 2. Digital images of the ***weathered oil*** observed in early 2011 from the ground in the Barataria Bay, LA. areas shown above.

scan lines acquired along the platform track allows the creation of a 2 dimensional image. The consequence of using this type of imaging system is that the scan lines collected produce spatial artifacts due to platform motion changes - resulting in scan line feature offsets. The following describes the roll induced problem to be corrected. Consider an airplane that is flying over a straight road indicated by the dark red, vertical line in the left image below. Now assume the airplane or mobile platform undergoes unwanted platform roll motion and thus the resulting straight feature in the acquired scene is curved, as suggested by the light, blue line in the left image. One knows that the road was straight so the image as shown in Figure 3 (right) indicates a lateral scan line adjustment is required in order to straighten the feature (the blue line). This is accomplished by "shifting" the scan lines opposite to the platform roll motion and results in an image where the feature in the image is corrected. Thus, one needs to calculate the offset that corresponds to the shift the pixels undergo.

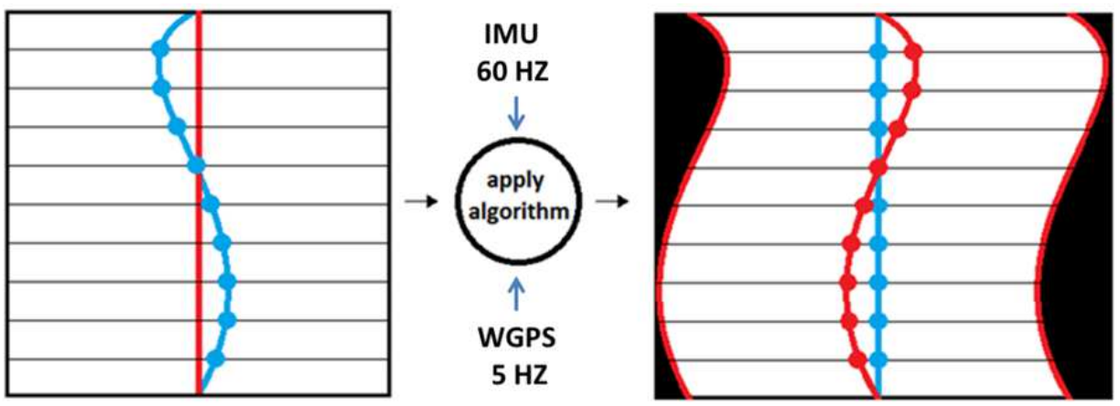

Fig. 3. The left figure shown in blue is a distorted road. The red line corresponds to the center of the scan line. The right image represents the corrected version of the left image. On this image the blue straight line is the road and the red curve is the actual position of the center pixels of the scan lines. In this example only the shift in the cross track direction is represented.

The offset mentioned previously can be corrected if sensing geometry and the hyperspectral imaging (HSI) system orientations are known when the different scan lines were taken. To obtain the platform and sensor orientation changes and position a 60 Hz update rate inertial measurement unit (IMU) was utilized and mounted to the gimbal mounted camera. An IMU is a device that is comprised of triads of accelerometers and gyroscopes. The accelerometers measure specific forces along their axes which are accelerations due to gravity plus dynamic accelerations. The gyroscopes measure angular rates. The IMU (Motion Node, GLI Interactive LLC, Seattle, Washington) that is used also has 3 magnetometers and outputs the orientation immediately by using those 3 types of sensors. In addition, differential WAAS 5 HZ GPS position, directional deviations, altitude with respect to a specified datum, and platform speed are collected during the flights.

An adaptive Kalman filter is used to estimate the induced platform motions using the combined sensor data from the GPS and IMU. The filtering technique thus allows one to

obtain the relative position of each scan line and the corresponding spatial pixel shift that needs to be applied to correct the image. When a gimbal mounted HSI pushbroom camera is used, there are two main influences that cause the geometric distortions. These are the slowly varying directional changes of the platform and the roll induced motions. The first step in the algorithm is to use the GPS to calculate the position of the sensor (O_x,O_y,O_z) at every scan line. The second step accounts for the influence of the roll motion by using the IMU sensor data. The position of a pixel on the earth's surface can be estimated using:

$$\begin{aligned} x &= Ox + \frac{s_x}{s_z}(h_{DEM} - Oz) \\ y &= Oy + \frac{s_y}{s_z}(h_{DEM} - Oz) \\ z &= h_{DEM} \end{aligned} \tag{1}$$

Where (S_x, S_y, S_z) are components of a unit central scan line ray vector, (x, y, z) the position in meters compared to the origin (the initial position of the center of the scan line) and h_{DEM} is the surface elevation given in meters with respect to Mean Sea Level (MSL).

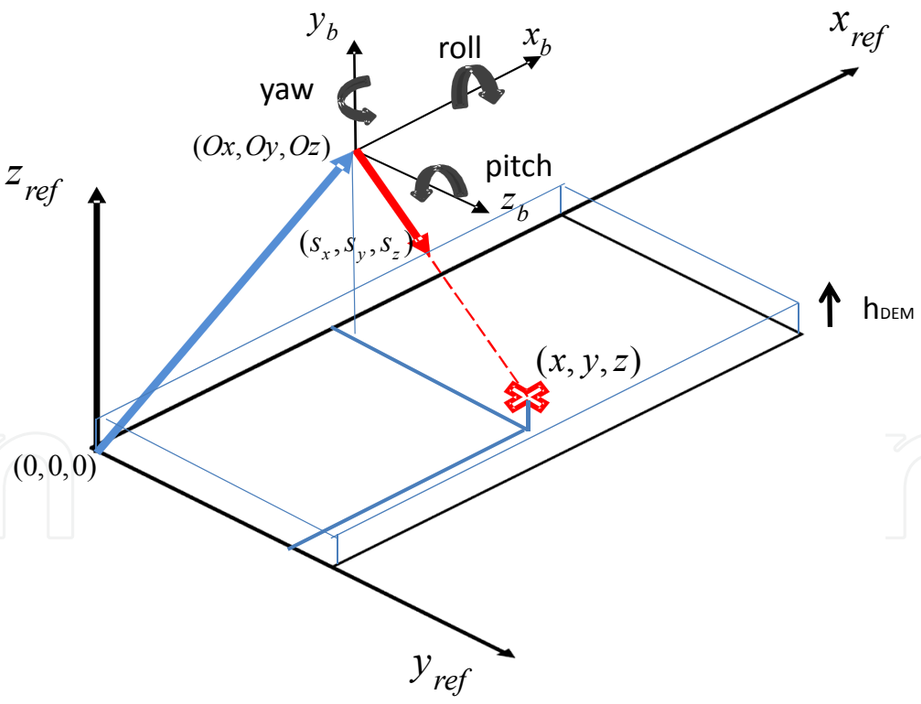

Fig. 4. This figure shows the position of the sensor (O_x, O_y, O_z) and the unit scan line ray vector in the reference coordinate system as well as the body (sensor platform) coordinate system with the possible platform motions. The position (x, y, z) is the position of the surface in the reference coordinate system that is located at the center of a HSI pixel .

The reference coordinate system chosen in this paper is a local tangent plane with the x axis pointed in the initial along track direction, y axis is 90 degrees clockwise to the x axis and corresponds to the initial cross track direction. In the results that are presented in this paper, shifts have only be applied in the cross-track direction. The shifts in meters are scaled to shifts in pixels as a function of the altitude (given by the GPS in meters), the field of view of the sensor (dependent upon the lens used) and the number of pixels in one scan line.

In the following section a description of the system is given, as well as the assumptions made. Then the application of the Kalman filter to acquire the position and velocity of the sensor is described with a detailed description of the vectors and matrices used. In the 2nd paragraph of this section, the influence of roll is taken into account. Then a paragraph that describes the image resampling phase applied to low flying airborne imagery in littoral areas.

In general, the application of the Kalman filter is used to acquire the position and velocity of the sensor is described with a detailed description of the vectors and matrices used and influence of roll is taken into account as described below, followed by a nearest neighbor resampling of the HSI imagery for each band independently.

Results that are presented in this paper, pixel shifts are only applied in the cross-track direction. Use of a gimbal sensor mount has allowed reduced HSI sensor motion corrections, however the need for improving image corrections in order to include pitch and yaw motions have been developed.

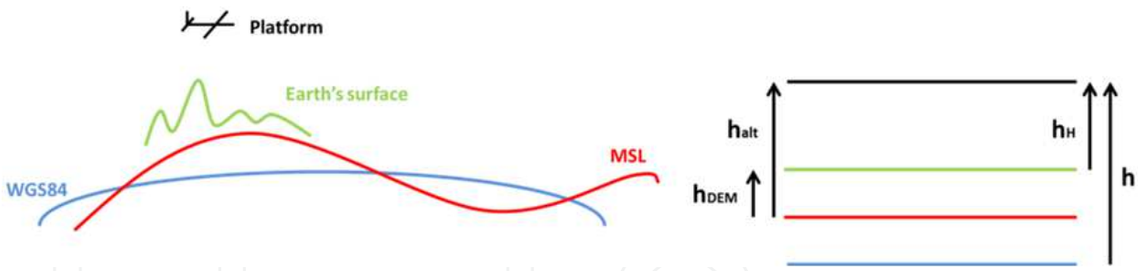

Fig. 5. This figure shows the different altitudes and heights used. Where h is the altitude of the platform with respect to the WGS84, h_{DEM} is the surface elevation, h_{alt} is the altitude of the platform with respect to MSL and h_H is the true altitude with respect to the earth's surface. In our applications we consider that the surface elevation is negligible as we take images of oil spills around MSL, so $h_H \approx h_{alt}$.

2.3 Description of the platform dynamic system

In order to model the movement of the platform, a discrete dynamic system described by the canonical state space equations are used:

$$\mathbf{x}_{k+1} = A_k \mathbf{x}_k + B_k \mathbf{u}_k + \mathbf{w}_k \tag{2}$$

$$\mathbf{z}_k = H_k \mathbf{x}_k + \mathbf{v}_k \tag{3}$$

where:

$\mathbf{x}_k$ = the state vector (6x1 matrix). $\mathbf{x}_k = (O_x\ O_y\ O_z\ V_x\ V_y\ V_z)_k^T$ contains the position of the sensor (O_x,O_y,O_z) (in meters) and the velocity (V_x,V_y,V_z) (in meters per second) in the reference coordinate system.
A_k = the (6x6) matrix that gives the relation between the previous state vector to the current state vector when no noise and no input vector are considered . This relation can also be given below by equation (4) for x, y and z.

$$(O_x)_{k+1} = (O_x)_k + (V_x)_k \tag{4}$$

where:
Δt_k = the time-interval (in seconds) between step k and k+1.
B_k = the (6xm) matrix that relates the optional input vector u to the current state. (m = the number of elements in the control input vector if external forces are considered).
$\mathbf{u}_k$ = the control input vector (mx1 matrix), we assume that there are no external forces that act upon the system so $\mathbf{u}_k$ =0 in our application. Actually, it is assumed that the drag is exactly compensated by the thrust and gravity by the lift.
$\mathbf{z}_k$ = the measurement vector (6x1 matrix). $\mathbf{z}_k$ = = $(O_{xm}\ O_{ym}\ O_{zm}\ V_{xm}\ V_{ym}\ V_{zm})_k^T$ contains the position of the sensor (O_{xm},O_{ym},O_{zm}) (in meters) and velocity (V_{xm},V_{ym},V_{zm}) (in meters per second) in the reference coordinate system obtained by the GPS.
H_k = the measurement sensitivity (6x6) matrix also known as the observation matrix that relates the state vector to the measurement vector ($\mathbf{z}_k = H_k\mathbf{x}_k$).
$\mathbf{w}_k$ = the process noise or also called dynamic disturbance noise (6x1 matrix) which is assumed white and Gaussian with covariance matrix Q_k (6x6 matrix).
$\mathbf{v}_k$ = the measurement noise of the GPS (6x1 matrix) which is also assumed white and Gaussian (detailed calculations of the covariances see below) and its associated covariance matrix R_k (6x6 matrix).

The subscript k refers to the time step at which the vector or matrix is considered and indicates the time dependence.

$\mathbf{x}_k$ contains the real position and velocity, whereas $\mathbf{z}_k$ contains the measured position and velocity. $\mathbf{z}_k$ is thus always prone to measurement noise.

In the first step, GPS data is used to calculate the position of the sensor (O_x,O_y,O_z) the matrices are defined as follows in the reference coordinate frame:

$$A_k = \begin{pmatrix} 1 & 0 & 0 & \Delta t & 0 & 0 \\ 0 & 1 & 0 & 0 & \Delta t & 0 \\ 0 & 0 & 1 & 0 & 0 & \Delta t \\ 0 & 0 & 0 & 1 & 0 & 0 \\ 0 & 0 & 0 & 0 & 1 & 0 \\ 0 & 0 & 0 & 0 & 0 & 1 \end{pmatrix}_k, \quad Q_k = \begin{pmatrix} 0.1 & 0 & 0 & 0 & 0 & 0 \\ 0 & 0.1 & 0 & 0 & 0 & 0 \\ 0 & 0 & 0.1 & 0 & 0 & 0 \\ 0 & 0 & 0 & 0.1 & 0 & 0 \\ 0 & 0 & 0 & 0 & 0.1 & 0 \\ 0 & 0 & 0 & 0 & 0 & 0.1 \end{pmatrix}_k$$

Detailed calculations of the covariance's σ_v^2 and σ_h^2 are respectively the covariance in vertical and horizontal position (in m^2) given by the GPS.

$$H_k = \begin{pmatrix} 1 & 0 & 0 & 0 & 0 & 0 \\ 0 & 1 & 0 & 0 & 0 & 0 \\ 0 & 0 & 1 & 0 & 0 & 0 \\ 0 & 0 & 0 & 1 & 0 & 0 \\ 0 & 0 & 0 & 0 & 1 & 0 \\ 0 & 0 & 0 & 0 & 0 & 1 \end{pmatrix}_k, \quad R_k = \begin{pmatrix} \frac{\sigma_h^2}{2} & 0 & 0 & 0 & 0 & 0 \\ 0 & \frac{\sigma_h^2}{2} & 0 & 0 & 0 & 0 \\ 0 & 0 & \sigma_v^2 & 0 & 0 & 0 \\ 0 & 0 & 0 & \frac{\sigma_{Vh}^2}{2} & 0 & 0 \\ 0 & 0 & 0 & 0 & \frac{\sigma_{Vh}^2}{2} & 0 \\ 0 & 0 & 0 & 0 & 0 & \sigma_{Vv}^2 \end{pmatrix}_k,$$

The covariance's of the vertical and horizontal velocities σ_{Vv}^2 and σ_{Vh}^2 (in m² per seconds²) are however not given by the GPS but are calculated using using the following, where:

A given quantity y is a function of x_1, x_2, … x_N given by the formula $y=f(x_1,x_2,...,x_N)$. The uncertainties in x_i are respectively e_1, e_2, …, e_N. The absolute uncertainty e_y is then given by

$$(e_y)^2 = \left(\frac{\partial f}{\partial x_1}\right)^2 (e_1)^2 + \left(\frac{\partial f}{\partial x_2}\right)^2 (e_2)^2 + ... + \left(\frac{\partial f}{\partial x_N}\right)^2 (e_N)^2$$

From the above, one has for the vertical, z direction $(V_z)_k = \frac{(O_z)_{k+1} - (O_z)_k}{\Delta t_k}$ and hence the covariance of the vertical velocity $(\sigma_{Vv}^2)_k$ equals $\frac{(\sigma_v^2)_{k+1} + (\sigma_v^2)_k}{\Delta t_k}$ since the velocity at time k equals the difference between the position at time k+1 and k, divided by the time interval. It is assumed that there is no uncertainty on the time interval. This is valid because one assumes that $\mathbf{x}_k$ and $\mathbf{x}_{k+1}$ are statistically independent. In an similar manner, one can calculate the covariance of the horizontal velocity, where one assumes

$$\sigma_{Ox}^2 = \sigma_{Oy}^2 = \frac{\sigma_h^2}{2} \text{ from } \sigma_h^2 = \sigma_{Ox}^2 + \sigma_{Oy}^2.$$

3. Kalman filter and smoothing approach

3.1 Position and velocity estimations

The Kalman filter consists of 2 steps. A temporal update step (also known as the "a priori" prediction step) and a measurement update step (also known as the "a posteriori" correction step). In the temporal step given by equations 4 and 5, the estimated state vector $\hat{\mathbf{x}}_k^-$ and the estimation covariance P_k^- at time step k are predicted based on the current knowledge at time step k-1.

The state vector $\hat{\mathbf{x}}_k$ contains the estimated position of the sensor (O_x,O_y,O_z) (in meters) and the velocity (V_x,V_y,V_z) (in meters per second) in the reference coordinate system.

The predictive procedure step is given by:

$$\begin{aligned} \hat{\mathbf{x}}_k^- &= A_{k-1}\hat{\mathbf{x}}_{k-1}^+ \\ P_k^- &= A_{k-1}P_{k-1}^+A_{k-1}' + Q_{k-1} \end{aligned} \tag{5}$$

and the measurement update step (given by equation 6 below) corrects the predicted estimated $\hat{\mathbf{x}}_k^-$ and P_k^- using the additional GPS sensor measurements $\mathbf{z}_k$ to obtain the corrected estimate of the state vector $\hat{\mathbf{x}}_k^+$ and P_k^+ or:

$$\begin{aligned} K_k &= P_k^-H_k'\left(H_kP_k^-H_k' + R_k\right)^{-1} \\ \hat{\mathbf{x}}_k^+ &= \hat{\mathbf{x}}_k^- + K_k\left(\mathbf{z}_k - H_k\hat{\mathbf{x}}_k^-\right) \\ P_k^+ &= \left(I - K_kH_k\right)P_k^- \end{aligned} \tag{6}$$

where, $\hat{\mathbf{x}}_k^-$ and $\hat{\mathbf{x}}_k^+$ are respectively the predicted (-) and corrected (+) value of the estimated state vector (6x1 vector), P_k^- and P_k^+ (a 6 x 6 matrix) are respectively the predicted and corrected value of the estimation covariance of the state vector, or:

$$P_k^+ = diag\left(\sigma_{Ox}^2, \sigma_{Oy}^2, \sigma_{Oz}^2, \sigma_{Vx}^2, \sigma_{Vy}^2, \sigma_{Vz}^2\right)_k$$

K_k (equation 6) is the Kalman gain (6x6 matrix).

The Kalman filter thus computes a weighted average of the predicted and the measured state vector by using the Kalman gain K_k. If one has an accurate GPS sensor, the uncertainty on the measurement will be small so there will be more weight given to the measurement and thus the corrected estimate will be close to the measurement. When one has a non-accurate sensor, the uncertainty on the measurement is large and more weight will be given to the predicted estimate.

A Kalman smoother has been applied as well where the equations are shown in (7) below. A Kalman Smoother in addition to the past observations also incorporates future observations to estimate the state vector:

$$\begin{aligned} C_k &= P_k^+A_k^T\left(P_{k+1}^-\right)^{-1} \\ \hat{\mathbf{x}}_k^s &= \hat{\mathbf{x}}_k^+ + C_k\left(\hat{\mathbf{x}}_{k+1}^s - A_k\hat{\mathbf{x}}_k^+\right) \\ P_k^s &= P_k^+ + C_k\left(P_{k+1}^s - P_{k+1}^-\right)C_k^T \end{aligned} \tag{7}$$

where:

$\hat{\mathbf{x}}_k^s$ = the smoothed estimated state vector (6x1 matrix).
P_k^s = the covariance (6x6) matrix of the smoothed estimated state vector.
C_k = the (6x6) matrix that determines the weight of the correction between the smoothed and non-smoothed state.

4. Roll correction

The second step in the algorithm for motion correction accounts for the influence of the roll motion by using the IMU orientation output. This is not included in the first Kalman filter because the IMU data is given at a higher frequency than the GPS data.

The state equations and Kalman filter/smoothing equations are given by 2.5, 2.6 and 2.7 with state vector $\hat{\mathbf{x}}_k'$ containing the estimated position of the center pixel of the scanline on the surface (in meters) and the tangent of the roll angle (nondimensional) in the reference coordinate system. The measurement vector $\mathbf{z}_k'$ contains the position of the sensor (O_x,O_y) (in meters) specified by the output of the previous Kalman filter in the reference coordinate system and the tangent of the rollangle r_m (nondimensional) given by the orientation output of the IMU.

The matrices used are defined by:

$$\mathbf{x}_k' = \begin{pmatrix} x \\ y \\ \tan r \end{pmatrix}_k, \quad A_k' = \begin{pmatrix} 1 & 0 & 0 \\ 0 & 1 & 0 \\ 0 & 0 & 1 \end{pmatrix}_k, \quad Q_k' = \begin{pmatrix} 0.1 & 0 & 0 \\ 0 & 0.1 & 0 \\ 0 & 0 & 0.001 \end{pmatrix}_k$$

$$\mathbf{z}_k' = \begin{pmatrix} O_x \\ O_y \\ \tan r_m \end{pmatrix}_k, \quad H_k' = \begin{pmatrix} 1 & 0 & 0 \\ 0 & 1 & h_{alt} \\ 0 & 0 & 1 \end{pmatrix}_k, \quad R_k' = \begin{pmatrix} \sigma_{Ox}^2 & 0 & 0 \\ 0 & \sigma_{Oy}^2 & 0 \\ 0 & 0 & \sigma_r^2 \end{pmatrix}_k$$

where:

r = the roll angle (in radians).
h_{alt} = the altitude of the sensor (in meters) with respect to MSL.
σ_{Ox}^2 and σ_{Oy}^2 = respectively the covariance of the position in x and y direction of the sensor given by the previous Kalman filter (in m^2).
σ_r^2 = the covariance of the roll angle given by the IMU (nondimensional).

5. Image resampling

In some cases, it is only desirable to cross-track shift corrections and not resample the image in order to keep the pure spectral signatures of measured pixels. Otherwise, 2D nearest neighbourhood resampling is used.

The cross-track shift corrections (which are in the y direction) s_s on the surface in meters need to be converted to pixelshifts s_p. The number of pixels in one scanline n_N, the altitude of the sensor above the surface in meters h_H and half of the angular field of view α are used. This is accomplished by defining a conversion ratio c_r, the shift in meters on the surface of 1 pixel shift, or:

$$c_r = \frac{w}{\frac{n_N}{2}} \tag{8}$$

where:

$w = h_H \tan \alpha$.

The pixelshift s_p is then given by $s_p = \frac{s_s}{c_r}$ as depicted below:

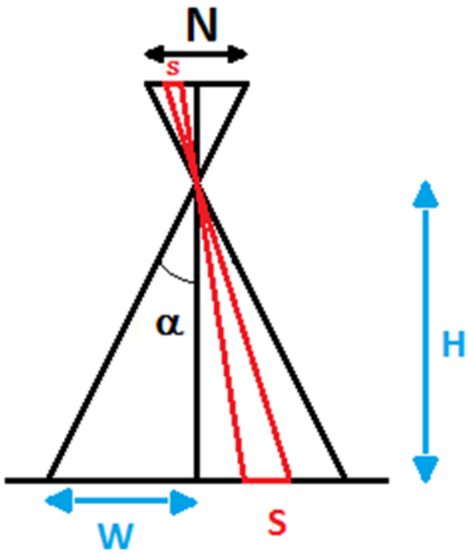

Fig. 6. This image shows the conversion triangles used to calculate the shiftratio between the shift on the earth surface s_s in meters and the pixelshift s_p. h_H is the altitude above the surface, α half of the angular field of view of the camera and n_N the number of pixels in one line.

6. Feature detection in hyperspectral images using optimal multiple wavelength contrast algorithms

Hyperspectral signatures and imagery offer unique benefits in detection of land and water features due to the information contained in reflectance signatures that directly show relative absorption and backscattering features of targets. The reflectance spectra that will be used in this paper were collected *in-situ* on May 31st 2011 using a SE590 high spectral resolution solid state spectrograph and the HSI imaging system described above. Bi-directional Reflectance Distribution Function (BRDF) signatures were collected of weathered oil, turbid water, grass and dead vegetation. The parameters describing the function in addition to the wavelength λ, (368-1115 nm) were the θ_i (solar zenith angle) = 71.5°, θ_0 (sensor zenith angle) = 55°, ϕ_i (solar azimuth angle) = 105° and the ϕ_0 (sensor azimuth angle) = 270°. The reflectance BRDF signature is calculated from the downwelling radiance using a calibrated Lambertian diffuse reflectance panel and the upwelling radiance at the above specified viewing geometry for each target (oil, water, grass, dead vegetation) as described in the figure below.

The figures below show the results of measurements from 400 to 900 nm for a 1 mm thick surface weathered oil film, diesel fuel, turbid water (showing the solar induced fluorescence line height feature, dead vegetation, and field grass with the red edge feature common to vegetation and associated leaf surfaces. These BRDF signatures are used below to select optimal spectral channels and regions using optimally selected contrast ratio algorithms in order to discriminate oil from other land & water features in hyperspectral imagery.

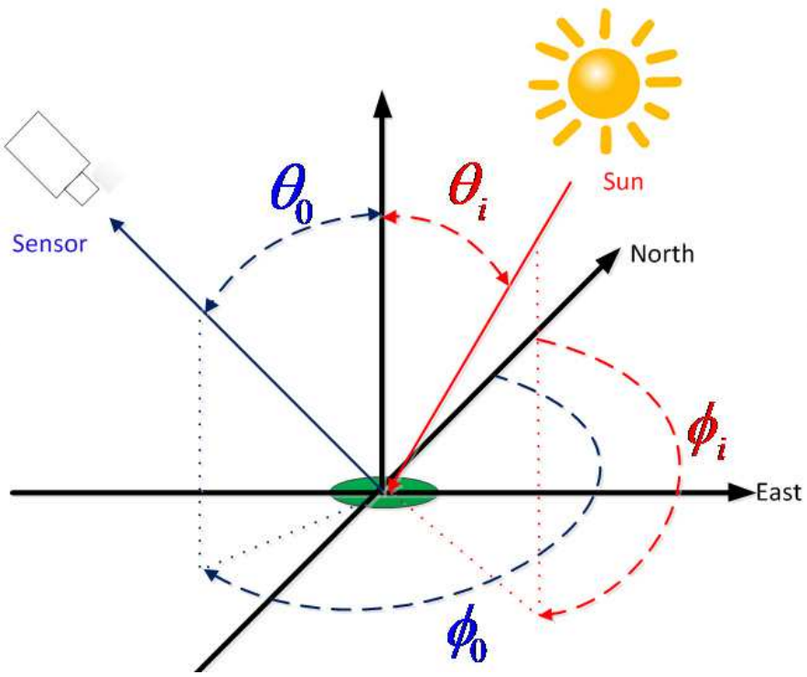

Fig. 7. Illumination and viewing geometry defined for calculation of the BRDF signatures collected using the 252 channel SE590 high spectral and radiometric sensitivity solid state spectrograph and the hyperspectral imaging system, where θ_i is the incident solar zenith angle of the sun, θ_0 is the sensor zenith angle, $\varnothing_i$ is the solar azimuth angle from the north and $\varnothing_0$ is the sensor azimuth angle as indicated above. In general, a goniometer measurement system is used to measure the BRDF in the field or laboratory environment as the sensor zenith and azimuth angles are changed during a collection period with a given solar zenith conditions.

The above BRDF signatures were used to select optimal spectral regions in order to apply the results to hyperspectral imagery collected from a weathered oil impacted shoreline in Barataria Bay, LA. The first method used was to perform feature detection using spectral contrast signature and HSI image contrast. The well know Weber's contrast definition is first used to determine the maximum (optimal) value of the contrast between a target *t* and a background *b* as a function of wavelength, or:

$$C_t(\lambda_k) = \frac{BRDF_t(\theta_0, \phi_0, \theta_i, \phi_i, \lambda_k) - BRDF_b(\theta_0, \phi_0, \theta_i, \phi_i, \lambda_k)}{BRDF_b(\theta_0, \phi_0, \theta_i, \phi_i, \lambda_k)} \tag{9}$$

The resulting contrast calculated across the spectrum for each channel are shown below using the 1 mm thick oil film as the target and the backgrounds of turbid water, dead vegetation (dead foliage), and field grass.

The result of the optimization of the contrast obtained from equation 9 yields an optimal channel and/or spectral region as a function of wavelength where the contrast is maximized between a specified target and specified background or feature in a hyperspectral image collected from a fixed or moving platform.

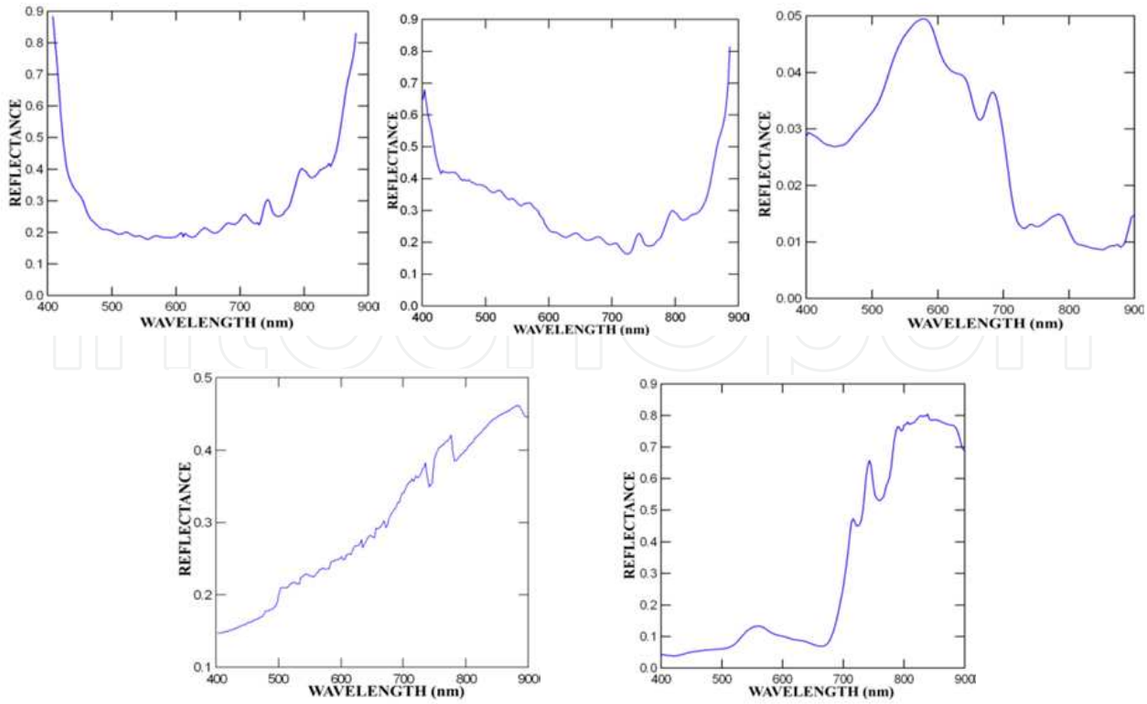

Fig. 8. Averaged (n=360) BRDF reflectance spectrums collected using a SE590 solid state spectrograph May 31, 2010. From upper left to right: BRDF spectrum of weathered oil (1 mm thick film) on clear water, diesel film (1mm thick film) on clear water, turbid water, with high chlorophyll content as indicated by the solar induced fluorescence line height, dead vegetation (dead leaves) and field grass showing the red edge. Solar angles were determined from DGPS location, time of day, and sensor position angles and measured angle from magnetic north direction.

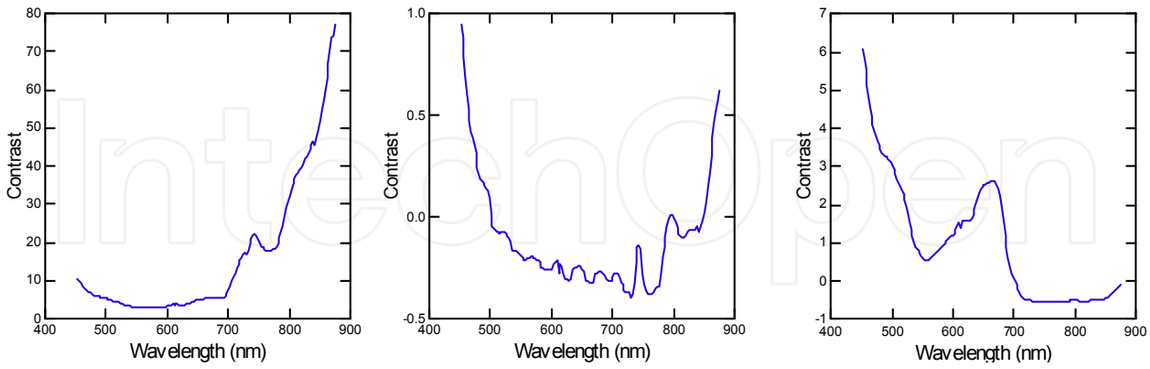

Fig. 9. Resulting BRDF Weber contrast signatures between oil as the target and different backgrounds (left to right): turbid water, dead vegetation (dead foliage) and field grass.

A limitation with this common definition of the contrast is that one band is used out of all the possible combinations available in a hyperspectral image for the feature detection or extraction algorithm. This limitation can be overcome, by defining an advantageous "*multiple-wavelength (or channel) contrast*" as:

$$C_t\left(\lambda_{k,m}\right)=\frac{BRDF_t\left(\theta_0,\phi_0,\theta_i,\phi_i,\lambda_k\right)-BRDF_b\left(\theta_0,\phi_0,\theta_i,\phi_i,\lambda_{k\pm m}\right)}{BRDF_b\left(\theta_0,\phi_0,\theta_i,\phi_i,\lambda_{k\pm m}\right)}$$
$$=\frac{BRDF_t\left(\theta_0,\phi_0,\theta_i,\phi_i,\lambda_k\right)}{BRDF_b\left(\theta_0,\phi_0,\theta_i,\phi_i,\lambda_{k\pm m}\right)}-1 \tag{10}$$

The result of the optimization of this "*multiple-wavelength contrast algorithm*" is the optimal selection of a band ratio (located in a spectral region) minus one. Furthermore, a new definition of the inflection contrast spectrum (a numerical approximation of the second derivative) can be defined. The contrast inflection spectrum described in previous papers was given by:

$$I_t\left(\lambda_{k,m,n}\right)=\frac{BRDF_t\left(\theta_0,\phi_0,\theta_i,\phi_i,\lambda_k\right)^2}{BRDF_t\left(\theta_0,\phi_0,\theta_i,\phi_i,\lambda_{k\pm m}\right)BRDF_t\left(\theta_0,\phi_0,\theta_i,\phi_i,\lambda_{k-n}\right)} \tag{11}$$

where m and n are respectively defined as a dilating wavelet filter forward and backward operators described by Bostater, 2006. This inflection is used to estimate the second derivative of reflectance spectra. The underlying goal of computing an approximation of the second derivative is to utilize the nonlinear derivative based, dilating wavelet filter to enhance the variations in the reflectance spectra signals, as well as in the contrast spectrum signals. These variations directly represent the target and background absorption (hence: concave up) and backscattering (hence: concave down) features within a hyperspectral reflectance image or scene and form the scientific basis of the discrimination based noncontact optimal sensing algorithms. A practical limitation encountered using this definition above, is that a concave-down (or backscattering) feature value of the inflection as defined in 2.7 is greater than one and a concave up (or absorption) feature, in the inflection or derivative based wavelet filter defined in 1.7 will be between 0 and 1. There is thus a difference in scale between a concave-up and a concave-down behavior. Consider the following example:

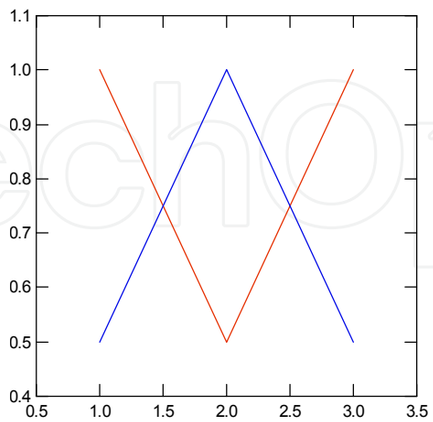

Fig. 10. Example concave-down (backscattering) feature (blue line) and a concave-up (absorption) feature (red line) of the same amplitude (Y axis) as a function of an spectral wavelength on the x axis.

In the case of the concave-down, the result of the inflection is:

$$I = \frac{1^2}{0.5 * 0.5} = 4$$

While in the case of the concave-up (same concavity), the result will be:

$$I = \frac{0.5^2}{1 * 1} = 0.25$$

To order to give equal weight to absorption and backscatter features in the band selection process, a modified spectrum for I*(λ) is defined as:

$$I^* = \begin{cases} I & for\ I > 1 \\ -\frac{1}{I} & for\ 0 < I < 1 \end{cases} \tag{12}$$

Using this definition, both concavities will be on the same scale and a concave-down feature (hence: backscattering) will give a positive value (>1) while a concave-up feature (hence: absorption) will give a negative value (<-1) and be treated the same numerically. For example, in the above example, the result for the new definition of the inflection or 2nd derivative estimator would be 4 and -4.

A second issue is to determine what values to assign to the upward and backward operators in the dilation filter. One could pick the optimal value for the inflection using all possible combinations of m and n. The problem with this method is that when m and n are large, the difference between the channels for which the inflection is calculated and the one to which it is compared can be influenced by the signal to noise ratio being at the low and high wavelengths in a typical camera/spectrograph system. Thus the resulting optimal regions selected can be scientifically or physically difficult to explain. Thus a limit is placed on the maximum value of the m, n operators from a practical point of view. The minimal value of m, n is 1. Thus, one can select the optimal range of the m and n wavelet filter operators (either a maximum (backscattering) or a minimum (absorption) for all combinations of m and n between 1 and the maximal value (in this paper this maximal value used was selected as 7). The resulting derivative estimator spectra (inflection spectra) using equation 12 was calculated and is shown below, using the previously shown BRDF spectra shown in Figure 8 above.

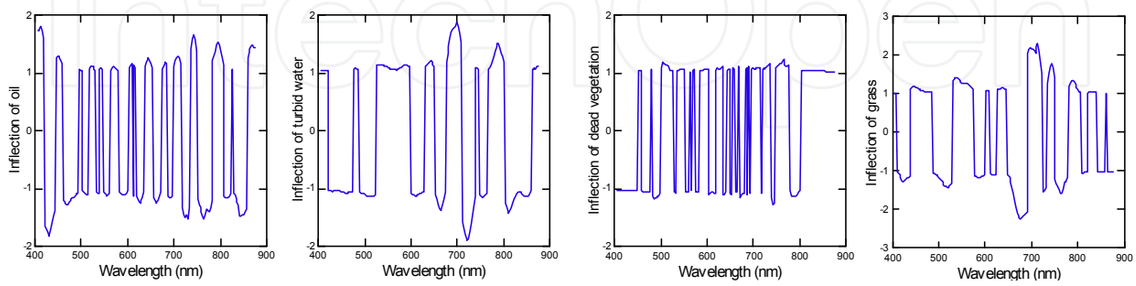

Fig. 11. BRDF Inflection spectra using the reflectance spectrums above. From left to right: an oil film (1mm thick) on clear water, turbid water, dead vegetation (dead leaves) and grass.

The inflection algorithm can also be applied to the contrast spectrums (to enhance variation in the contrast spectrum). The result of this calculation is given in the following figures.

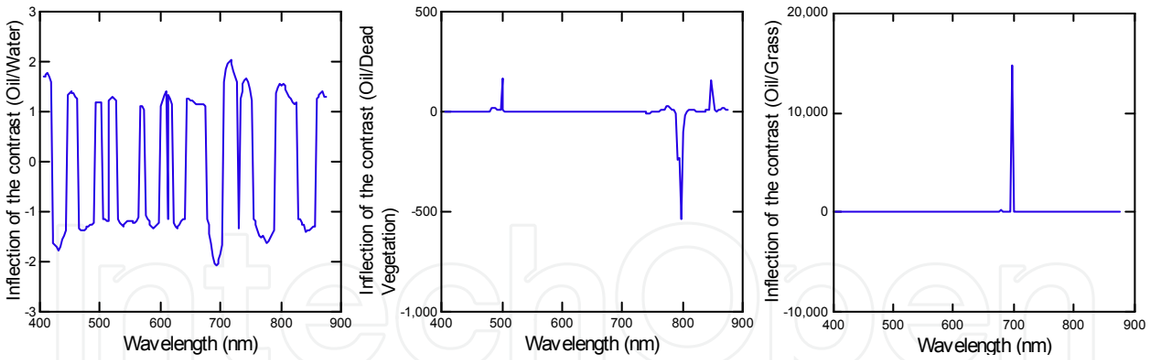

Fig. 12. Inflection of the contrast spectra. The contrast target is weathered oil with different backgrounds. From left to right: turbid water, dead vegetation (dead leaves) and grass are the contrast backgrounds.

Once the inflection spectra are calculated, it is also possible to apply Weber's definition of the contrast to the inflection spectra instead of the BRDF. The resulting contrast spectrums are given in the following figure:

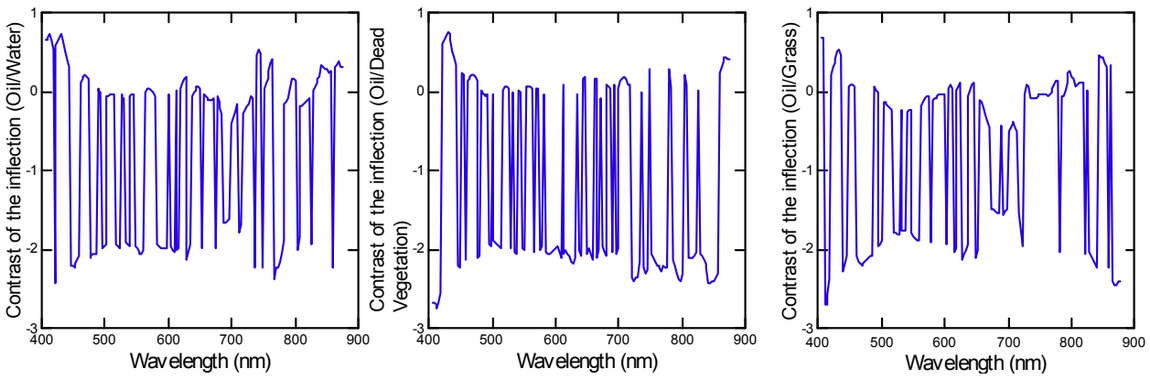

Fig. 13. Weber contrast of the inflection spectra. The target is weathered oil with different backgrounds. From left to right: turbid water, dead vegetation (dead leaves) and grass. Optimal bands and spectral regions are indicated by the greatest positive or negative values across the spectrums.

The result of the optimization procedures yields a band or band ratio for the different types of contrast (Weber's contrast, contrast of the inflection or inflection of the contrast). The optimal bands using the different techniques that were obtained using weathered oil film as the target and water, dead vegetation or grass as backgrounds are shown in the Table 1, and are used in processing hyperspectral imagery collected using the methods in the results section of this paper (see Table 1).

7. Collection of hyperspectral imagery from littoral zone

In order to detect and discriminate the presence of weathered oil on a near shore habitat or the spatial extent of weathered oiled along a shoreline, a novel and new technique has been developed for collecting HSI imagery from a small vessel (anchored or underway), or the sensor mounted in the littoral zone. The resulting HSI imagery produces pixel sizes or ground

sampling distances (GSD) on the order of several mm to cm scales, depending upon the distance between the sensor and the shoreline. The purpose of collecting this type of imagery is to (1) reduce atmospheric affects and (2) minimize the influence of the "mixed pixel" and "adjacency effects" in selecting spectral regions for detection of weathered oil and for testing algorithms. The results are also immediately and directly applicable to low altitude airborne imagery, especially if the same sensor is used aboard the airborne platform.

	Water	Mud and oil	Sand	Vegetation
Weber's contrast	$Band(\lambda = 759\text{nm})$	$Band(\lambda = 378\text{nm})$	$Band(\lambda = 368\text{nm})$	$Band(\lambda = 345\text{nm})$
Inflection of the contrast	$Band(\lambda = 382\text{nm})$	$Band(\lambda = 360\text{nm})$	$Band(\lambda = 382\text{nm})$	$Band(\lambda = 710\text{nm})$
Contrast of the inflection	$Band(\lambda = 420\text{nm})$	$Band(\lambda = 684\text{nm})$	$Band(\lambda = 424\text{nm})$	$Band(\lambda = 684\text{nm})$
Multiple wavelength contrast	$\frac{Band(\lambda = 454nm)}{Band(\lambda = 345nm)} - 1$	$\frac{Band(\lambda = 751nm)}{Band(\lambda = 345nm)} - 1$	$\frac{Band(\lambda = 751nm)}{Band(\lambda = 345nm)} - 1$	$\frac{Band(\lambda = 751nm)}{Band(\lambda = 345nm)} - 1$
Multiple wavelength contrast of the inflection	$Band(\lambda = 394nm)$ $-Band(\lambda = 363nm)$	$Band(\lambda = 394nm)$ $-Band(\lambda = 363nm)$	$Band(\lambda = 394nm)$ $-Band(\lambda = 363nm)$	$Band(\lambda = 394nm)$ $-Band(\lambda = 363nm)$

Table 1. Resulting bands or band ratios for the optimization of: the contrast (Weber's definition), the inflection of the contrast, the contrast of the inflection spectra, the multiple wavelength contrast (as defined above) and the multiple wavelength contrast of the inflection spectra. In each case, weathered oil is the target and the background is: water, mixture of oil and mud, sand or vegetation.

The sensor used to view the shoreline can be directly mounted on the vessel or can be mounted above the water but near the shore using a tripod or in a vessel. In the case of a mounted sensor on a vessel, the vessel is anchored at two points, allowing movement in mainly one direction (for example the boat is anchored to mainly allow motion due to waves in the pitching direction. Fixed platform mounting does not require motion correction, however the data collected from the anchored vessel requires roll motion correction (in this case pitch correction).

In order to perform this correction, an IMU (inertial measurement unit) is attached to the HSI sensor and collects the sensor motion information while the pushbroom sensor sweeps or is rotated (using a rotation stage) along the shoreline being investigated. This correction will be applied before any further processing of the contrast algorithms are applied to the imagery taken in the Northern Gulf of Mexico and shown below. An example of the measurement scheme that has been used to detect and discriminate weathered oil (as described above) is shown below.

The image below (right) is the resulting hyperspectral image 3 band RGB display of a shoreline that has been impacted by a recent oil-spill in the Gulf of Mexico region, near Bay Jimmy, Louisiana.

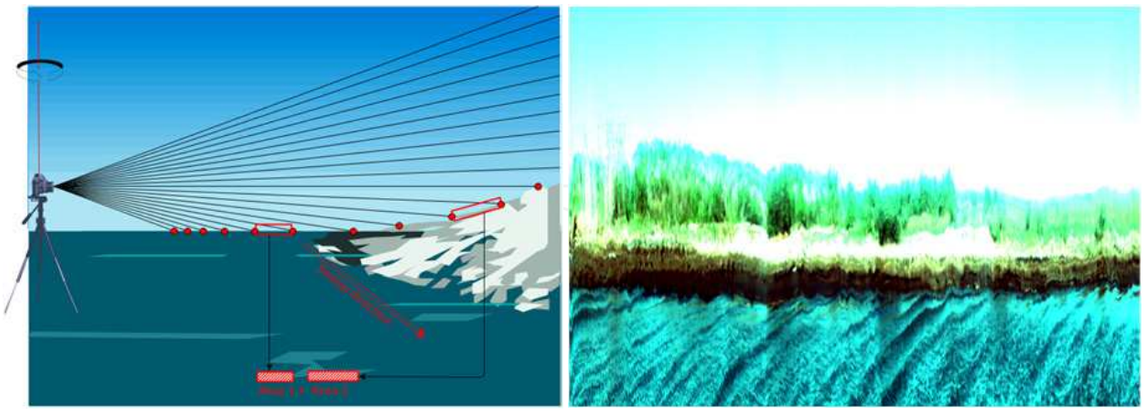

Fig. 14. The HSI imaging system (left) is placed upon a small vessel or a fixed platform (tripod) in shallow water types within viewing distance of a shoreline. The sensor sweeps the shoreline and the pushbroom sensor produces a hyperspectral image of the shoreline as shown in the above HSI 3 band image (right). Note the ability to see gravity and capillary waves, small grasses on the shoreline as well as weathered oil at the land-water margin. Image collected February 28, 2011 in Barataria Bay, Louisiana

In this case a vessel mounted sensor was used and the image was corrected for the platform motion (right). To illustrate the influence of the motion of a small vessel, and the necessary IMU corrections needed, a shoreline was imaged from a vessel (below left image) and from a fixed *in-situ* platform (right image) in April 2011 the platform motion (right).

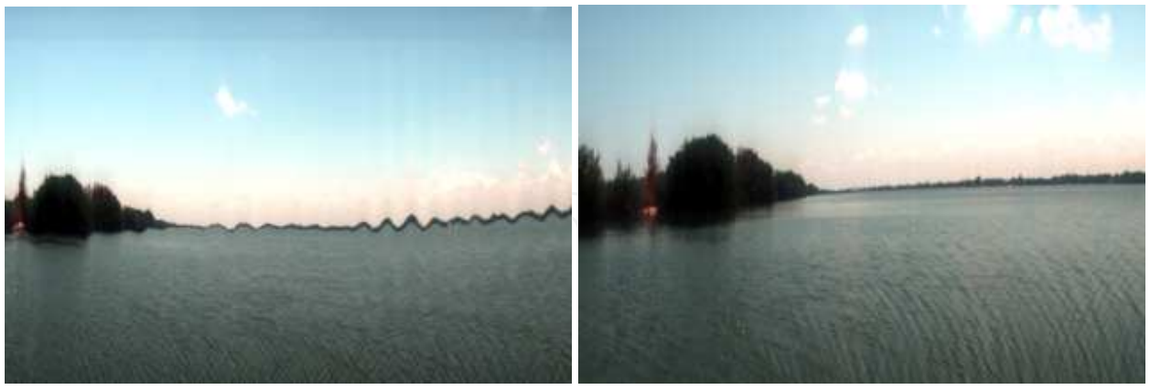

Fig. 15. A hyperspectral image (left) 3 band RGB display of a littoral zone using a pushbroom sensor mounted on a vessel anchored at two points. During the acquisition of the hyperspectral image the sensor records the pitching effect of the anchored vessel that needs to be corrected using an IMU sensor due to the water surface gravity waves. The influence of this motion can clearly be seen in the image if no correction is applied (left). The shoreline area (right) acquired when the pushboom sensor was mounted on fixed platform above the water. In this case no correction needs to be applied to the image. Note the clarity of the water surface capillary and small gravity waves.

8. Conclusion

The purpose of this paper has been to describe different calibration approaches and techniques useful in the development and application of remote sensing imaging systems. Calibration includes the use of laboratory and field techniques including the scanning of photogrammetric negatives utilized in large format cameras, as well as *in-situ* targets and spectral wavelength and radiance calibration techniques. A newly integrated hyperspectral airborne pushbroom imaging system has been described in detail. Imagery from different integrated imaging systems were described for airborne remote sensing algorithm developments using high spatial resolution (on the order of a few mm^2 to larger sub meter pixel sizes) imaging systems. The high spatial and spectral resolution imagery shown in this paper are examples of technology for characterization of the water surface as well as subsurface features (such as weathered oil) in aquatic systems.

Other ongoing applications in the Marine & Environmental Optics Lab making use of data from the remote sensing systems described in this paper are (a) land surface vegetation studies needed for ongoing climate change studies currently being conducted in coastal Florida scrub vegetation studies and (b) layered radiative transfer modeling of surface and subsurface oil signatures for sensor comparisons and related algorithm development to detect surface and subsurface oil using spectral and spatial data fusion and sharpening techniques.

9. Acknowledgments

The work presented in this paper has been supported in part by the Northrop Grumman Corporation, NASA, Kennedy Space Center, KB Science, the National Science Foundation, the US-Canadian Fulbright Program, and the US Department of Education, *FIPSE* & European Union's grant *Atlantis STARS* (Sensing Technology and Robotics Systems) to Florida Institute of Technology, the Budapest University of Engineering and Economics (BME) and the Belgium Royal Military Academy, Brussels, in order to support of the involvement of undergraduate students in obtaining international dual US-EU undergraduate engineering degrees. Acknowledgement is also given to recent funding from the Florida Institute of Oceanography's BP Corporation's research grant award in support of aerial image acquisition.

10. References

Aktaruzzaman, A., [Simulation and Correction of Spectral Smile Effect and its Influence on Hyperspectral Mapping]. MS Thesis, International Institute for Geo-Information Science and Earth Observation, Enschede, Netherlands, pp. 77 (2008)

Bostater, C., "Imaging Derivative Spectroscopy for Vegetation Dysfunction Assessments", SPIE Vol. 3499, pp. 277-285 (1998)

Bostater, C., Ghir, T., Bassetti, L., Hall, C., Reyier, R., Lowers, K., Holloway-Adkins, K., Virnstein, R., "Hyperspectral Remote Sensing Protocol for Submerged Aquatic Vegetation in Shallow Water", SPIE Vol. 5233, pp. 199-215 (2003)

Bostater, C., Jones. J., Frystacky, H., Kovacs, M., Joza, O., "Image Analysis for Water & Subsurface Feature Detection In Shallow Waters", SPIE Vol. 7825, pp. 7825-17-1 to 7, (2010).

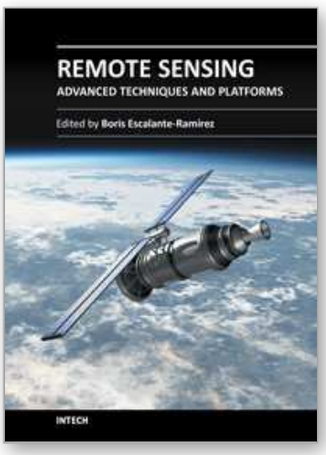

Remote Sensing - Advanced Techniques and Platforms
Edited by Dr. Boris Escalante

ISBN 978-953-51-0652-4
Hard cover, 462 pages
Publisher InTech
Published online 13, June, 2012
Published in print edition June, 2012

This dual conception of remote sensing brought us to the idea of preparing two different books; in addition to the first book which displays recent advances in remote sensing applications, this book is devoted to new techniques for data processing, sensors and platforms. We do not intend this book to cover all aspects of remote sensing techniques and platforms, since it would be an impossible task for a single volume. Instead, we have collected a number of high-quality, original and representative contributions in those areas.

InTech Europe
University Campus STeP Ri
Slavka Krautzeka 83/A
51000 Rijeka, Croatia
Phone: +385 (51) 770 447
Fax: +385 (51) 686 166
www.intechopen.com

InTech China
Unit 405, Office Block, Hotel Equatorial Shanghai
No.65, Yan An Road (West), Shanghai, 200040, China
中国上海市延安西路65号上海国际贵都大饭店办公楼405单元
Phone: +86-21-62489820
Fax: +86-21-62489821

IntechOpen